

Supplementary Data and Appendix for:

Separation of hemodynamic signals from GCaMP fluorescence measured with widefield imaging

Valley M.T.*¹, Moore M. G.*², Zhuang J¹, Mesa N¹, Castelli D¹, Sullivan D¹,
Reimers M², Waters J¹

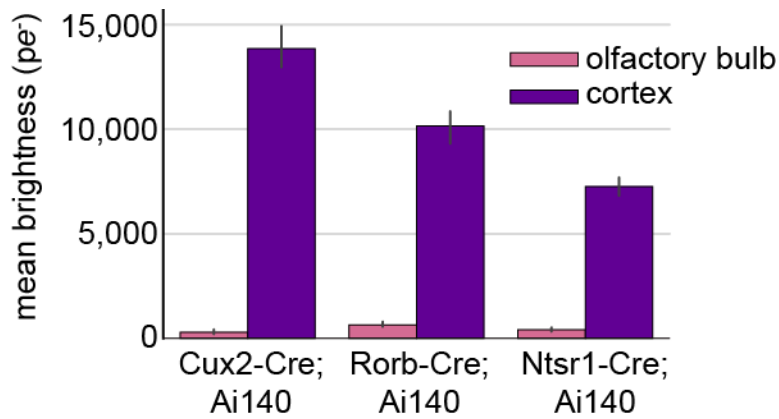


Fig S1. Relative brightness of GFP mice.

Image brightness, in mean photoelectrons, calculated from 10x10 pixel regions (65.0 μm^2) over medial somatosensory cortex from 3 Cux2-Ai140, 3 Rorb-Ai140 and 5 Ntsr1-Ai140 mice. Olfactory bulb measurements were taken to represent the background photon count, including tissue autofluorescence, skull autofluorescence, and light leak.

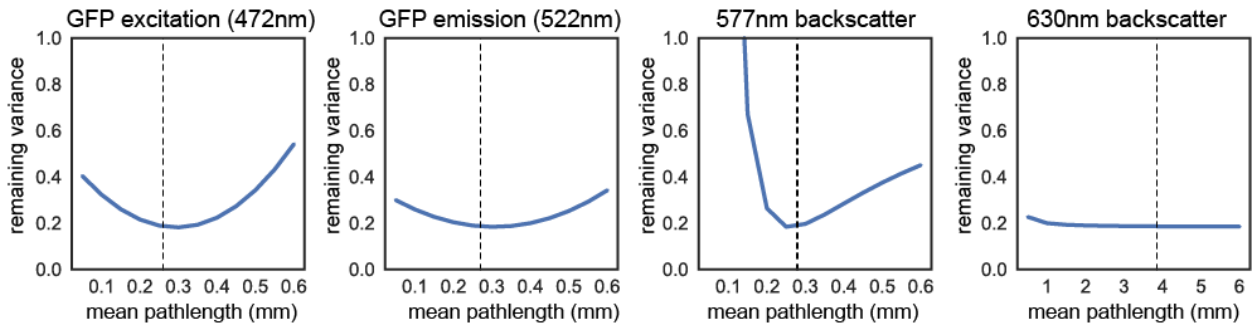


Fig S2. Sensitivity of Beer-Lambert model to changes in path length.

The median remaining variance of all pixels across the brain from a single Cux2-Cre;Ai140 mouse while changing one mean path length in the Beer-Lambert model. The sensitivity of model performance to each path length was evaluated with all other parameters (including other path lengths) constant. Path lengths values used elsewhere in the paper are marked with dotted lines: 260 μ m (GFP excitation), 270 μ m (GFP emission), 280 μ m (577nm backscatter), 3.85mm (630nm backscatter).

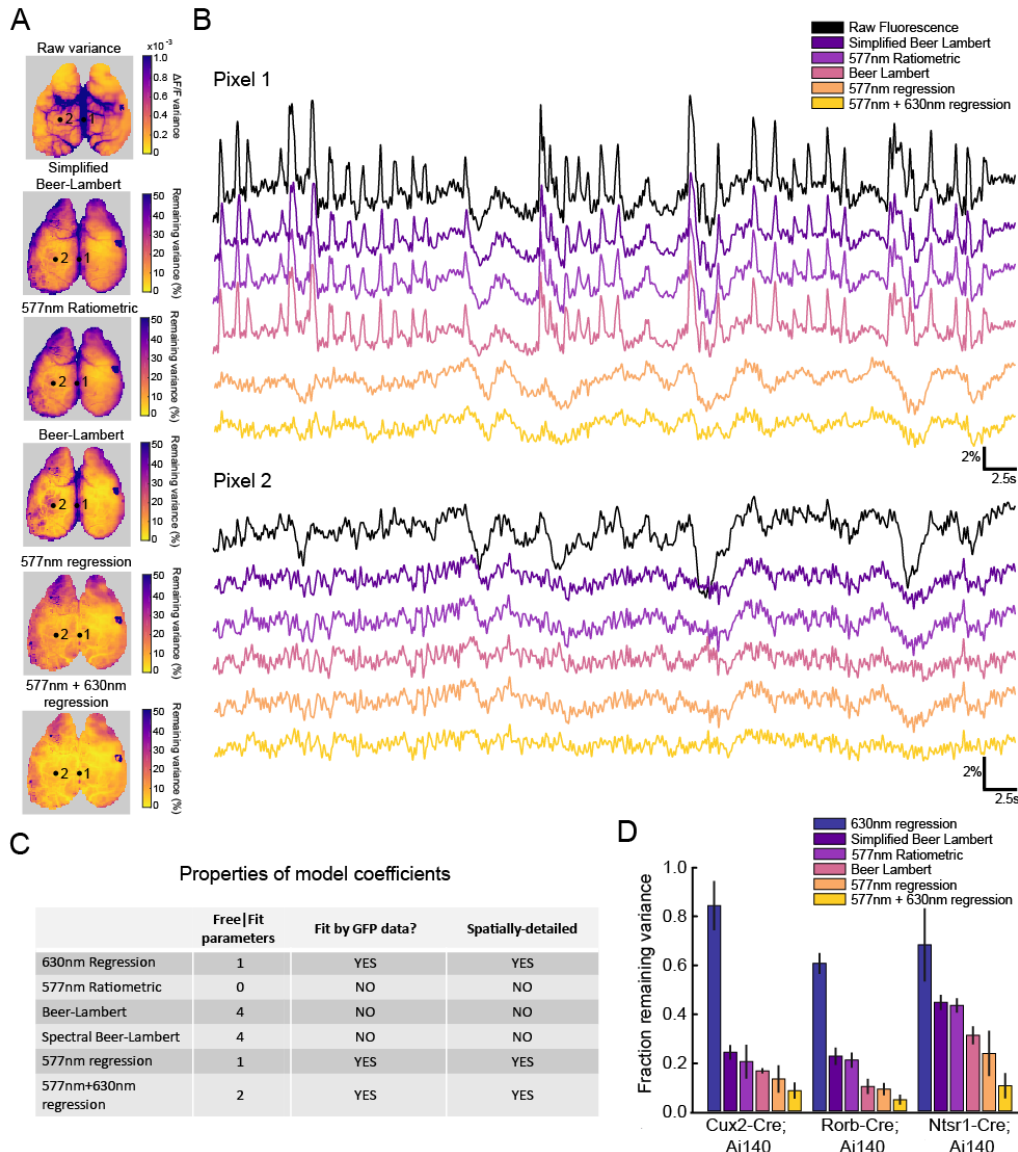


Fig S3. Detailed comparison of all models against GFP results.

(A) Map of variance from a Cux2-Ai140 (GFP) mouse (top), and maps of remaining variance after correction using 5 models. (B) Example traces of spontaneous activity and corrected traces from two example pixels (dots, left). Raw data was corrected using five methods: Simplified Beer Lambert (see supplemental appendix), Ratiometric demixing ($((1+dF/F) / (1+dR_{577nm}/R_{577nm}))$), Beer-Lambert demixing (see supplemental appendix), 577nm regression (Eq. 9 omitting the term for S_2), and 577nm + 640nm regression (Eq. 9). (C) Summary of key differences between how coefficients are generated in the five models. (D) Summary of variance remaining after correction (averaged across cortical surface) from three Cre lines. Bars in D represent mean \pm STD. 3 Cux2-Ai140 mice, 3 Rorb- Ai140 mice, 5 Ntsr1-Ai140 mice.

A

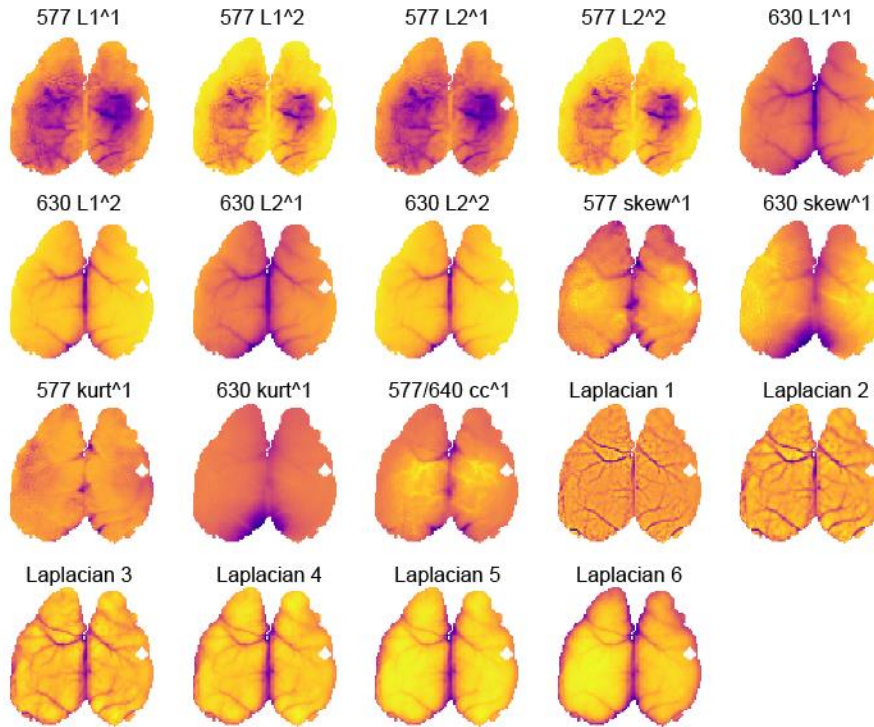


Fig S4. Maps of Spatial Model regressors.

(A) 19 different projections of backscatter data (or fluorescence data for Laplacian maps) were used as regressors in the Spatial Model to predict coefficient maps from GFP-expressing mice. Statistical maps are: the L1 norm of $\Delta I_1/\bar{I}_1$ and its square, the L2 norm (standard deviation) of $\Delta I_1/\bar{I}_1$ and its square, the L1 norm of $\Delta I_2/\bar{I}_2$ and its square, the L2 norm of $\Delta I_2/\bar{I}_2$ and its square, the skewness of the 577nm and 630nm signals, the kurtosis of the 577nm and 630nm signals, the covariance of $\Delta I_1/\bar{I}_1$ and $\Delta I_2/\bar{I}_2$, the Laplacian maps. Images from a Cux2-Ai140 mouse.

	577 L1^1	577 L1^2	577 L2^1	577 L2^2	630 L1^1	630 L1^2	630 L2^1	630 L2^2	577 skew^1	630 skew^1	577 kurt^1	630 kurt^1	577/630 cc^1	Lap 1	Lap 2	Lap 4	Lap 8	Lap 16	Lap 32	Mean
Cux2 577	-0.704	0.401	0.281	-0.095	-2.999	0.565	3.166	-0.524	-0.006	-0.049	-0.058	-0.295	0.023	-0.022	0.026	-0.001	0.024	0.238	0.098	1.443
Cux2 630	-0.416	0.204	0.340	-0.172	-0.573	-0.435	0.892	0.221	-0.056	-0.075	-0.053	-0.025	-0.013	0.046	-0.066	0.129	-0.398	0.162	0.071	-0.850
Rorb 577	-2.091	0.161	1.146	0.468	1.016	-2.041	-1.334	2.401	0.082	-0.023	-0.094	-0.121	-0.140	0.016	-0.059	-0.113	0.489	-0.075	0.109	1.600
Rorb 630	0.583	0.936	-0.435	-1.148	0.916	-0.845	-0.503	0.693	-0.140	-0.138	0.050	0.089	-0.059	0.031	-0.048	0.272	-0.760	0.222	0.201	-0.832
Ntsr1 577	6.668	-4.153	-7.559	4.855	-1.988	0.646	1.978	-0.578	-0.040	-0.052	0.170	-0.348	-0.027	0.032	-0.194	0.455	-0.633	0.642	0.010	1.981
Ntsr1 630	1.118	-0.186	0.167	-0.612	5.967	-2.082	-5.601	1.884	0.014	-0.156	0.124	0.585	-0.039	0.143	-0.236	0.574	-1.555	1.083	-0.112	-1.729

Supplementary Table 1. Tabulated coefficients for the Spatial Model.

Weights for all spatial-coefficients, each representing the mean weight for the mouse line.

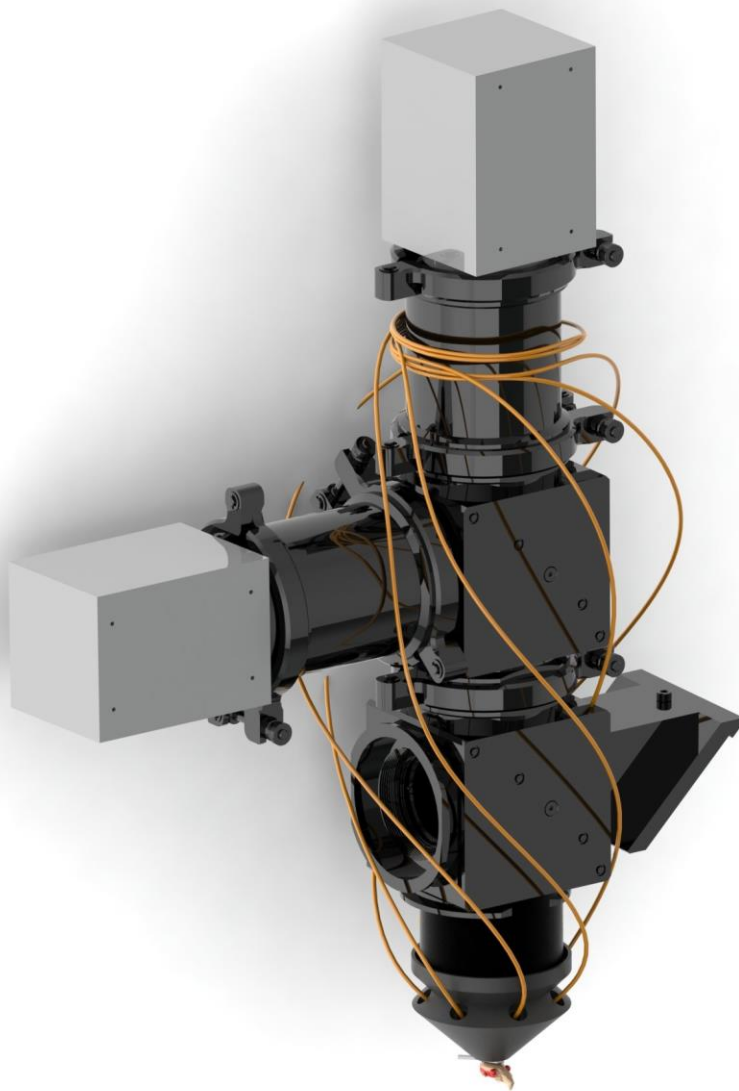


Fig S5. Custom widefield optics system. A modular filter-cube was designed to align cameras, objectives and 2" optics (see also fig 2C for schematic of the optical system). Radial off-axis illumination of mouse cortex for backscatter imaging used a custom light-shield receiving seven LED-coupled optical fibers (LEDs not shown), while epifluorescence excitation enters through the open port in the bottom cube.

APPENDIX

Derivation of the Beer-Lambert and Regression models

A coarse-grained hemodynamic model for the fluorescence intensity recorded from a single pixel, $I_F(t)$, based on the Beer-Lambert Law and general principles of incoherent optical processes, can be written in compact form as

$$I_F(t) = F(t)T_{em}(\mathbf{c}(t))T_{ex}(\mathbf{c}(t))I_{ex}^S, \quad (A1)$$

where $F(T)$ is the coarse-grained intrinsic activation level of the fluorophores averaged over the PSF of the pixel, $T_{em}(\mathbf{c}(t))$ is the transmittance factor for the light emitted by the fluorophores, $T_{ex}(\mathbf{c}(t))$ is the transmittance factor for the excitation light, and I_{ex}^S is the excitation source intensity at the specific pixel. The transmittances depend on the oxygenated and deoxygenated hemoglobin concentrations, $C_{HbO}(t)$ and $C_{HbR}(t)$, respectively, can be combined into a 2-component vector, $\mathbf{c}(t) = [C_{HbO}(t), C_{HbR}(t)]$. Likewise, the recorded intensity of the b^{th} backscatter channel can be expressed

$$I_b(t) = T_b(\mathbf{c}(t))I_b^S, \quad (A2)$$

where $T_b(\mathbf{c}(t))$ is the round-trip transmittance, and I_b^S is the corresponding source intensity.

The transmittance factors, $T_\mu(\mathbf{c}(t))$, where $\mu \in \{em, ex, b\}$, can be written as

$$T_\mu = \mathcal{G}_\mu \int d\lambda dx X_\mu(x|\lambda)P_\mu(\lambda)e^{-x \cdot \mathbf{c}(t) \cdot \mathbf{e}(\lambda)}, \quad (A3)$$

where \mathcal{G}_μ contains any geometric factors for the corresponding process, $X_\mu(x|\lambda)$ is the distribution over optical path lengths for a given wavelength, λ , and $P_\mu(\lambda)$ is the distribution over wavelengths for the process, including source spectra, filters, and fluorophore excitation/emission spectra, as required. While traveling along a given path, the light is subject to absorption by hemoglobin, in accordance with the Beer-Lambert Law. This is described by the exponential factor in equation 3, which contains the path-length, x , the hemoglobin concentrations, $\mathbf{c}(t)$ and $\mathbf{e}(\lambda) = [E_{HbO}(\lambda), E_{HbR}(\lambda)]$, a two-component vector containing the corresponding hemoglobin molar-extinction coefficients for wavelength λ .

The model has 3 dynamic variables, $F(t)$, $C_{HbO}(t)$, and $C_{HbR}(t)$, which can be expressed in terms of mean-values and deviations as $F(t) = \bar{F} + \Delta F(t)$ and $C_v(t) = \bar{C}_v + \Delta C_v$, where $v \in \{HbO, HbR\}$. In the limit where the deviations are small compared to the mean values, as is often the case with wide-field calcium imaging using bright indicator dyes, we can linearize the equations relating the observed intensities to the intrinsic variables. Linearization permits simplification by eliminating some variables. To linearize equations (1) and (2), we first express the intensities as a mean value plus deviation, $I_F(t) = \bar{I}_F + \Delta I_F(t)$, and $I_b(t) = \bar{I}_b + \Delta I_b(t)$. This leads to

$$\bar{I}_F + \Delta I_F = (\bar{F} + \Delta F) T_{em}(\bar{c} + \Delta c) T_{ex}(\bar{c} + \Delta c) I_{ex}^S, \quad (A4)$$

$$\bar{I}_b + \Delta I_b = T_b(\bar{c} + \Delta c) I_b^S. \quad (A5)$$

The transmittances can be expanded to first-order in terms of the hemoglobin fluctuations as

$$T_\mu(\bar{c} + \Delta c) \approx T_\mu(\bar{c}) + \left(\frac{\partial T_\mu(\bar{c})}{\partial \bar{c}_{HbO}} \right) \Delta C_{HbO} + \left(\frac{\partial T_\mu(\bar{c})}{\partial \bar{c}_{HbR}} \right) \Delta C_{HbR}. \quad (A6)$$

Inserting this expansion into equations (4) and (5), and equating the zeroth order terms with respect to the fluctuations gives the mean intensities

$$\bar{I}_F \approx \bar{F} T_{em}(\bar{c}) T_{ex}(\bar{c}) I_{ex}^S, \quad (A7)$$

$$\bar{I}_b \approx T_b(\bar{c}) I_b^S. \quad (A8)$$

Similarly, equating first-order terms, and dividing by the mean gives

$$\frac{\Delta I_F(t)}{\bar{I}_F} = \frac{\Delta F(t)}{\bar{F}} + (M_{em,HbO} + M_{ex,HbO}) \Delta C_{HbO}(t) + (M_{em,HbR} + M_{ex,HbR}) \Delta C_{HbR}(t), \quad (A9)$$

$$\frac{\Delta I_b(t)}{\bar{I}_b} = M_{b,HbO} \Delta C_{HbO}(t) + M_{b,HbR} \Delta C_{HbR}(t), \quad (A10)$$

with

$$M_{\mu, \nu} = \frac{1}{T_\mu(\bar{c})} \left(\frac{\partial T_\mu(\bar{c})}{\partial \bar{c}_\nu} \right) = - \frac{\int d\lambda \, dx \, X_\mu(x|\lambda) P_\mu(\lambda) e^{-x \bar{c} \cdot e(\lambda)} x E_\nu(\lambda)}{\int d\lambda \, dx \, X_\mu(x|\lambda) P_\mu(\lambda) e^{-x \bar{c} \cdot e(\lambda)}}, \quad (A11)$$

where again $\mu \in \{em, ex, b\}$ and $\nu \in \{HbO, HbR\}$.

The spectral distributions for the light-sources for the fluorescence indicators and for the camera acceptance filters are readily obtained, as are the hemoglobin molar extinction coefficients. The path length distributions and mean hemoglobin molar concentrations, on the other hand, can vary from pixel to pixel and would need to be measured or estimated for each pixel in the field of view.

Because there are two independent hemoglobin components, a minimum of two reflectance channels are necessary to separate the fluorescence from hemodynamics. With a single fluorescence intensity, $I_F(t)$, and two backscatter channels, $I_1(t)$ and $I_2(t)$, equation (5) then becomes a pair of backscatter equations,

$$\frac{\Delta I_1(t)}{\bar{I}_1} = M_{1,HbO} \Delta C_{HbO}(t) + M_{1,HbR} \Delta C_{HbR}(t), \quad (A13)$$

$$\frac{\Delta I_2(t)}{\bar{I}_2} = M_{2,HbO} \Delta C_{HbO}(t) + M_{2,HbR} \Delta C_{HbR}(t). \quad (A14)$$

These equations can be solved for the hemodynamic variables, giving

$$\Delta C_{HbO}(t) = \frac{1}{M_{1,HbO}M_{2,HbR} - M_{1,HbR}M_{2,HbO}} \left(M_{2,HbR} \frac{\Delta I_1(t)}{\bar{I}_1} - M_{1,HbR} \frac{\Delta I_2(t)}{\bar{I}_2} \right), \quad (A15)$$

$$\Delta C_{HbR}(t) = \frac{1}{M_{1,HbO}M_{2,HbR} - M_{1,HbR}M_{2,HbO}} \left(-M_{2,HbO} \frac{\Delta I_1(t)}{\bar{I}_1} + M_{1,HbO} \frac{\Delta I_2(t)}{\bar{I}_2} \right). \quad (A16)$$

These results can be inserted into the equation for $\Delta I_F/\bar{I}_F$, giving

$$\frac{\Delta I_F(t)}{\bar{I}_F} = \frac{\Delta F(t)}{\bar{F}} + S_1 \frac{\Delta I_1(t)}{\bar{I}_1} + S_2 \frac{\Delta I_2(t)}{\bar{I}_2}, \quad (A17)$$

where the coefficients are given by

$$S_1 = \frac{(M_{em,HbO} + M_{ex,HbO})M_{2,HbR} - (M_{em,HbR} + M_{ex,HbR})M_{2,HbO}}{M_{1,HbO}M_{2,HbR} - M_{1,HbR}M_{2,HbO}}, \quad (A18)$$

$$S_2 = \frac{-(M_{em,HbO} + M_{ex,HbO})M_{1,HbR} + (M_{em,HbR} + M_{ex,HbR})M_{1,HbO}}{M_{1,HbO}M_{2,HbR} - M_{1,HbR}M_{2,HbO}}. \quad (A19)$$

Extending this formalism to the entire image, we arrive at the final formula

$$\frac{\Delta F(x, y, t)}{\bar{F}(x, y)} = \frac{\Delta I_F(x, y, t)}{\bar{I}_F(x, y)} - S_1(x, y) \frac{\Delta I_1(x, y, t)}{\bar{I}_1(x, y)} - S_2(x, y) \frac{\Delta I_2(x, y, t)}{\bar{I}_2(x, y)}. \quad (A20)$$

The coefficients, S_1 and S_2 , generalize to maps, $S_1(x, y)$ and $S_2(x, y)$, because the mean hemoglobin concentrations and optical path-length distributions can in principle vary from pixel to pixel.

Simplified Beer-Lambert Model: path length and wavelength approximation

There are two major approximations that can be used to simplify the calculations of the backscatter regression coefficients, S_1 and S_2 . The first is to replace the distribution over path lengths with a single

characteristic path length, $x_c(\lambda)$. This is accomplished by taking $X(x|\lambda) \rightarrow \delta(x - x_c(\lambda))$, where $\delta(x)$ is the Dirac delta function. The second approximation is to replace the distribution over wavelengths with a single characteristic wavelength, λ_c , accomplished by taking $P(\lambda) \rightarrow \delta(\lambda - \lambda_c)$.

Taking these two approximations together gives

$$S_1 = \frac{E_{Hbo}(\bar{\lambda}_{em})E_{Hbr}(\bar{\lambda}_2) - E_{Hbr}(\bar{\lambda}_{em})E_{Hbo}(\bar{\lambda}_2)}{E_{Hbo}(\bar{\lambda}_1)E_{Hbr}(\bar{\lambda}_2) - E_{Hbr}(\bar{\lambda}_1)E_{Hbo}(\bar{\lambda}_2)} \left[\frac{x_{em}}{x_1} \right] + \frac{E_{Hbo}(\bar{\lambda}_{ex})E_{Hbr}(\bar{\lambda}_2) - E_{Hbr}(\bar{\lambda}_{ex})E_{Hbo}(\bar{\lambda}_2)}{E_{Hbo}(\bar{\lambda}_1)E_{Hbr}(\bar{\lambda}_2) - E_{Hbr}(\bar{\lambda}_1)E_{Hbo}(\bar{\lambda}_2)} \left[\frac{x_{ex}}{x_1} \right], \quad (A21)$$

$$S_2 = \frac{E_{Hbr}(\bar{\lambda}_{em})E_{Hbo}(\bar{\lambda}_1) - E_{Hbo}(\bar{\lambda}_{em})E_{Hbr}(\bar{\lambda}_1)}{E_{Hbo}(\bar{\lambda}_1)E_{Hbr}(\bar{\lambda}_2) - E_{Hbr}(\bar{\lambda}_1)E_{Hbo}(\bar{\lambda}_2)} \left[\frac{x_{em}}{x_2} \right] + \frac{E_{Hbr}(\bar{\lambda}_{ex})E_{Hbo}(\bar{\lambda}_1) - E_{Hbo}(\bar{\lambda}_{ex})E_{Hbr}(\bar{\lambda}_1)}{E_{Hbo}(\bar{\lambda}_1)E_{Hbr}(\bar{\lambda}_2) - E_{Hbr}(\bar{\lambda}_1)E_{Hbo}(\bar{\lambda}_2)} \left[\frac{x_{ex}}{x_2} \right], \quad (A22)$$

which is the result from (Ma et al. 2016a).

Using our images from GFP mice, we can invalidate this simplification of the Beer-Lambert model (equations 21, 22) for the wavelengths used in our experiment (see figure S3 for remaining variance). Using our wavelengths ($\lambda_{ex} = 473.23$ nm, $\lambda_{em} = 519.99$ nm, $\lambda_1 = 577.20$ nm, and $\lambda_2 = 630.30$ nm), and path lengths (577nm: 280 μ m, 630nm: 3.85mm, 472nm: 260 μ m for one-way fluorophore excitation, 522nm: 270 μ m for one-way fluorescent emission, Ma *et al.*, 2016a), equation (22) predicts a positive value for S_2 ($S_1 = 1.0314$, $S_2 = 0.1289$), whereas after regression our data yields a negative value over 99.53% of pixels (see figure 3E). A positive value for S_2 can only be obtained from Eqs. (21) and (22) for our wavelengths by taking one of the backscatter path lengths to be negative. Hence this simplification of the Beer-Lambert model requires the use of path lengths that are not physically plausible.

Spectrally-detailed Beer-Lambert Model

The alternative to the path length and wavelength approximation of the simplified Beer-Lambert model is to replace the path length distributions with single characteristic path lengths ($X(x|\lambda) \rightarrow \delta(x - x_c(\lambda))$) equation 11, but to keep the integral over wavelengths and the exact forms of the various spectral distributions $P_\mu(\lambda)$. When applied to our data from GFP mice, with the wavelength integrals computed numerically, this level of approximation results in the correct signs for the backscatter coefficients, S_1 and S_2 , so that it is possible to adjust the path-lengths and obtain agreement between the experimental data

and the Beer-Lambert model. This is the form of the Beer-Lambert model used in this paper (see figure 3).

To compute the coefficients in this manner requires estimates for the background oxy- and deoxy-hemoglobin concentrations. If the molar concentration of hemoglobin in mouse blood is 2.2×10^{-3} mol/L (Raabe *et al.*, 2011), with a typical oxygenation level of 85%, and a Cortical Blood Volume in mouse cortex of ~ 0.04 (Chugh *et al.*, 2008), we arrive at $\hat{C}_{HbO} 7.4 \times 10^{-5}$ mol/L and $\hat{C}_{HbR} 1.3 \times 10^{-5}$ mol/L. We note that the results are insensitive to these numbers, e.g. the dependence vanishes altogether in the approximations (21) and (22). Changing the values over the entire plausible range only changes the resulting coefficients in the third significant figure, hence these reasonable estimates are sufficient.

We apply this to our experimental setup by computing the wavelength integrals in (11) numerically, using directly measured spectra for the two back-scatter channels, combined with manufacturers spectra for our GFP filter, and GFP fluorophore spectra from (<http://www.tsienlab.ucsd.edu/Documents.htm>). We also use extinction coefficient data from (<http://omlc.org/spectra/hemoglobin/summary.html>), and estimated path-lengths from (Ma *et al.*, 2016a). This leads to the coefficients ($S_1=1.176$, $S_2=-0.434$) which corresponds closely to the regression coefficients calculated in the absence of physical estimates (figure 3E). This shows that a negative 640nm regression coefficient can be obtained from Beer-Lambert with positive path-lengths, and results from the details of the wavelength dependence of the extinction coefficients and path-length data. This is the form of the Beer-Lambert model used in this paper (figure 3).

Spatial-Regression Model

Correction of hemodynamics in GCaMP mice presents a challenge for our regression approach because in these animals the fluorescent signal, $\Delta I_F / \bar{I}_F$, contains an unknown calcium-dependent signal, $\Delta F / \bar{F}$ term (Eq. (7), main text). Because of neurovascular coupling, the hemodynamic and calcium-dependent terms are not independent so that a simple regression of $\Delta I_1 / \bar{I}_1$ and $\Delta I_2 / \bar{I}_2$ from $\Delta I_F / \bar{I}_F$ will not yield the true calcium dynamic signal.

For a GFP mouse, the coefficient maps, $S_1(x, y)$ and $S_2(x, y)$ are obtained by pixel-wise linear regression of the fluorescence signal onto the backscatter signals. To transfer the obtained maps between different mice, we first correlate the features in the maps with corresponding features in the individual brain structures. To do this we constructed a set of $M=19$ maps, $M_m(x, y)$, where $m \in \{1, 2, \dots, M\}$, from the backscatter data and fluorescence data. These maps should be chosen so that they do not reflect calcium dynamics when they are obtained from a GCaMP mouse. Because the data is scaled by the mean-intensities on each channel before any models are constructed, these maps should also be dimensionless and not scale with intensity.

The statistical maps we use are: [1-2] the L1 norm of $\Delta I_1/\bar{I}_1$ and its square, [3-4] the L2 norm of $\Delta I_1/\bar{I}_1$ and its square, [5-6] the L1 norm of $\Delta I_2/\bar{I}_2$ and its square, [7-8] the L2 norm of $\Delta I_2/\bar{I}_2$ and its square, [9-10] the skewness of the 577nm and 630nm signals, [11-12] the kurtosis of the 577nm and 630nm signals, [13] the covariance of $\Delta I_1/\bar{I}_1$ and $\Delta I_2/\bar{I}_2$. To capture the location of the blood-vessels independently of the excitation intensity profile, we compute the ratio of a Gaussian-blurred time-averaged image of the fluorescence emission divided by the time-averaged image itself. Rather than choose a blurring length-scale arbitrarily, we include maps computed at multiple blurring length-scales. The remaining 6 maps are blood-vessel maps computed for length scales of 1, 2, 4, 8, 16, and 32 pixels, respectively (Laplacian maps, figure S4).

We include in our training datasets only those pixels whose fractional variance explained (FVE) is above a chosen threshold of 75%. This is because a low FVE was found to reflect pixels whose initial variance is very low, roughly the same as that obtained on high FVE pixels after demixing, so that the model is fitting noise rather than signal on those pixels.

We constructed three types of Spatial Models: (1) standard Spatial Models, (2) cross-validated Spatial Models, and (3) Cre line Spatial Models.

Standard Spatial Model: the 19 maps are z-scored across pixels for a single GFP animal and merged into a $19 \times D_{\text{TRAIN}}$ predictor array, P_{TRAIN} , where D_{TRAIN} is the number of pixels in the training set (i.e. $\text{FVE} > .75$). The two direct-regression coefficient maps, S_1 and S_2 for the same set of pixels are merged into a $2 \times D_{\text{TRAIN}}$ response array, R_{TRAIN} , for the same animal. From a linear regression model, $R_{\text{TRAIN}} - \langle R_{\text{TRAIN}} \rangle = C_{\text{MM}} - P_{\text{TRAIN}}$, where $\langle \dots \rangle$ indicates average over pixels, we obtain the 2×19 coefficient array, C_{MM} . We can then reconstruct the response data as $R_{\text{MM}} = C_{\text{MM}} \cdot P_{\text{TEST}} + \langle R_{\text{TRAIN}} \rangle$, where P_{TEST} contains the 19 z-scored predictors from all pixels in the same animal. R_{MM} is then used to demix the fluorescence from the animal, so that the remaining variance can be compared to the optimal result obtained by direct backscatter regression. In this way, we can learn how much error is introduced by the process of transferring the backscatter-regression coefficient maps onto the 19-map representation.

Cross-validated Spatial-Model: This model is used to test the amount of error caused by transferring the spatial-model coefficients from one animal to another. For each animal, we again obtain a reconstructed response array, $R_{\text{MMCV}} = C_{\text{MMCV}} \cdot P_{\text{TEST}} + \langle R_{\text{TRAIN}} \rangle$, but here C_{MMCV} is obtained from a training set consisting of all training pixels ($\text{FVE} > .75$) from all other animals in the same Cre line (i.e. the test animal is excluded from the training data). The testing set then consists of all pixels in the test animal. Here the differential between remaining variance obtained by demixing the fluorescence signal with R_{MMCV} and that obtained via R_{MM} in the same GFP mouse estimates the error incurred during transfer of the spatial-model between animals.

Cre-line-wise Spatial Model: Here the training set consists of all training pixels ($FVE > .75$) in all animals in a Cre line. The trained model is then expected to be used to construct the backscatter coefficients for all pixels in a GCaMP mouse. This would represent the best attempt to demix the GCaMP animal using all available training data from the same Cre line. Error limits would come from the cross-validated GFP results, with the caveat that in the case of small cohorts, including the additional animal in the training data will presumably lower the error somewhat, meaning that the cross-validation results are likely an overestimate of the Spatial Model error.